



Influence of sub-surface deformation induced by machining on stress corrosion cracking in lead-free brass

Jakob Johansson¹ · Volodymyr Bushlya¹ · Charlotta Obitz² · Rachid M'Saoubi^{1,3} · Joacim Hagström⁴ · Filip Lenrick¹

Received: 16 May 2022 / Accepted: 2 September 2022 / Published online: 13 September 2022
© The Author(s) 2022

Abstract

New stricter regulations on lead (Pb) content in brass for use in certain applications is driving the industry from traditional leaded brass towards Pb-free alloys. However, machining induced surface integrity for such Pb-free alloys and related corrosion resistance are largely unknown. Two Pb-free brass alloys, CuZn38As and CuZn21Si3P, approved for use in drinking water applications, were machined under different cutting conditions, tool geometries and tool wear states. The resulting surface integrity and sub-surface deformation was characterized using nano-indentation, scanning electron (SEM) and ion microscopy, and electron backscatter diffraction (EBSD). The materials resistance to stress corrosion cracking (SCC) was assessed by exposing the machined samples to a corrosive substance in accordance with SIS 117102. The results show that tool wear is the most influencing parameter leading to stronger sub-surface deformation. This was especially pronounced for alloy CuZn38As, where for equivalent depth of deformation, the material exhibited higher degree of work-hardening compared to the other tested alloy. Subsequently, substantial stress corrosion cracking was registered for machined CuZn38As samples.

Keywords Machining · Brass alloys · Sub-surface deformation · Stress corrosion cracking

1 Introduction

Brass is a commonly used engineering material for components where high corrosion resistance is desired, such as couplings and pipe fittings in water handling systems. Traditionally, brass has been alloyed with lead (Pb) to improve machinability and castability of the material [1, 2]. Due to its detrimental effects on living organisms and the environment, Pb is restricted in applications with a risk of Pb leaching, e.g. drinking water applications [3, 4]. Since the use of Pb-containing alloys will be further restricted in the near future [5], Pb-free alloys are gaining popularity in the manufacturing industry.

Machining Pb-free brass is associated with higher cutting forces, severe tool wear and less chip control as compared to machining leaded brass [6, 7, 8, 9]. Since tool wear is a known contributing factor to increased sub-surface deformation [10], and more aggressive tool wear is observed when machining Pb-free brass alloys, a higher degree of sub-surface deformation is expected in Pb-free brass alloys. It is therefore of interest to investigate the influence of cutting data and tool geometry variation with wear on sub-surface deformation and its link to stress corrosion cracking (SCC). Sub-surface deformation is part of surface integrity, as introduced by Field and Kahles [11, 12], and can have large influence on a components service life.

Stress corrosion cracking is a severe problem that can lead to components underperforming or even catastrophic failure. For brass products in drinking water systems, SCC causes leakage of water and creates risks of extensive damages to surrounding structures [13]. SCC involves crack formation due to simultaneous effects of static tensile stresses and corrosion. The factors behind SCC can be divided into environmental factors, metallurgical factors and mechanical stress and strain [14]. Stress corrosion cracking is primarily associated with aqueous ammonia when it comes to

✉ Jakob Johansson
Jakob.Johansson@iprod.lth.se

¹ Division of Production and Materials Engineering, Lund University, Lund, Sweden

² RISE Research Institutes of Sweden, Stockholm, Sweden

³ R&D Materials and Technology Development, Seco Tools AB, Fagersta, Sweden

⁴ Stainless Steels & Non-Ferrous Metals, Swerim, Stockholm, Sweden

brass alloys. Cracking of copper components after exposure to ammonia was reported already in the beginning of the twentieth century [15]. However, SCC can be caused by a wide variety of species including sulphates, nitrates, nitrites, chloride containing species and pure water [16]. Alloy composition, especially zinc concentration, and material heat treatment practices have shown to impact the material susceptibility to SCC, [16]. The tensile stress may originate from external load or as residual stresses induced by cold working, machining, welding or heat treatment [16]. Initiation sites are often either pits formed by pitting, or deposit corrosion or as defects caused by forming and machining [16].

In machining, the removal of material is associated with three separate and distinct deformation zones around the cutting tool [17]. While primary and secondary deformation zones are associated with the chip formation and tool-chip interface, the tertiary deformation zone is formed by the contact between the machined surface and the tool clearance side. This tertiary deformation zone, directly related to surface integrity, remains in the finished machined surface and defines its performance in an application. Assessment of a relationship between machining-induced surface integrity and product performance is a routine procedure for components operating in critical applications, and is well documented for Ni- and Ti-based alloys [18, 19], and stainless steels [20, 21]. Literature about surface integrity of machined copper alloys [19] and brass alloys is available [22, 23], and knowledge regarding SCC in brass also exist [24, 25, 26]. However, no studies on the connection between machining induced surface integrity and SCC could be found in the case of brass. Therefore, this paper investigates the surface integrity response to different machining conditions and tool wear conditions for two common Pb-free alloys and correlates the sub-surface deformation to stress corrosion cracking.

2 Experimental setup

Two brass alloys that are approved to be used in drinking water applications, CuZn38As and CuZn21Si3P, are chosen for the study, and their chemical composition is shown in Table 1. The materials have different microstructures; CuZn38As is a single-phase material that mainly consists of the α -phase, with only trace amounts of the β -phase from the

binary Cu–Zn system. The microstructure for CuZn21Si3P is more complex; it contains the same α -phase as CuZn38As, as well as a so-called κ' -phase. The κ' -phase is similar to the κ -phase found in the binary Cu–Si phase system with regard to atomic arrangement but has slightly different lattice parameters, and it is stable at room temperature. These aspects of microstructure for the materials were revealed using Electron Backscatter Diffraction (EBSD) and X-Ray Diffraction (XRD) as seen in Fig. 1.

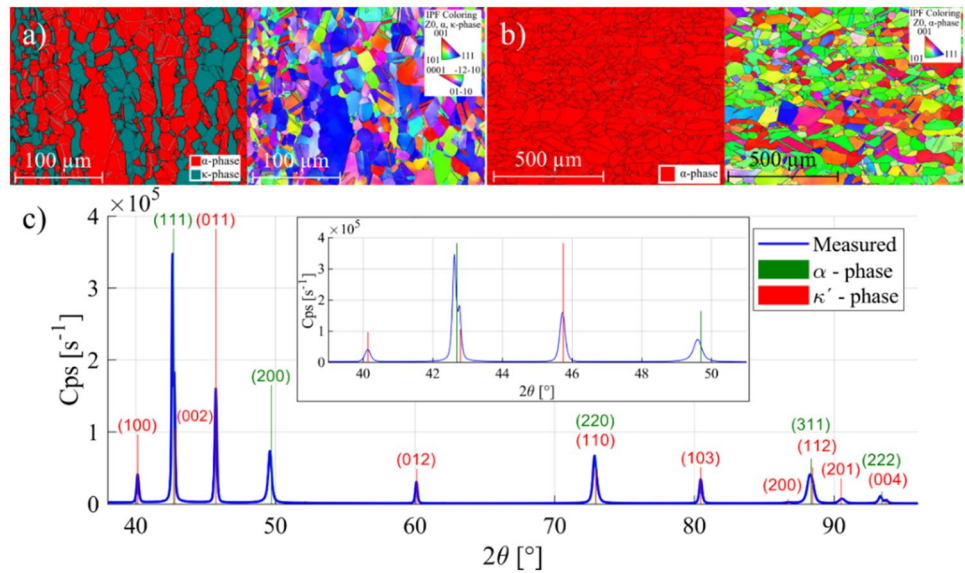
The cutting conditions chosen for generating the machined samples were similar to conditions at brass component manufacturing facilities. The samples were produced in a longitudinal turning operation. The depth of cut, a_p , and cutting speed, v_c , were kept constant at 2 mm and 200 m/min, respectively, while the feed rate, f , was varied in three levels: 0.05, 0.15 and 0.4 mm/rev. Since tool wear is a major contributor to sub-surface deformation, a worn tool with flank wear, $VB = 0.37$ mm, as well as an unworn tool with small edge radius and a large positive rake angle ($\gamma = 22.5^\circ$), was used to produce high and low levels of deformation, see Fig. 2. The tool holder DCLNL3225P12-M was used for both the sharp insert, which was of ISO CCGT120408F-AL, KX geometry and the worn tool, which was originally of ISO CNMG120408-MF1 geometry. Both inserts were of uncoated cemented carbide. The profiles of the edge lines, shown in Fig. 2, were measured using a 3D-optical microscope, Alicona Infinite Focus G4, and each edge profile in Fig. 2 represents an average of 500 measurements on the tools in the study. As can be seen in the cutting edge profiles in Fig. 2, both new and worn tool have similar rake angle with the flank wear being the main difference.

Nano-indentation and Electron Backscatter Diffraction (EBSD) were used to quantify the depth of the sub-surface deformation and the degree of the deformation. In nano-indentation, a diamond Berkovich tip is indented into the material with a small load, in this case 10 mN, and the hardness is evaluated based on the load–displacement curve [27]. The small size of the imprints, approximately 0.2 – 0.5 μm deep, enables high spatial resolution. Prior to indentation the samples were sectioned, ground and fine-polished. The NanoTest Vantage system by MicroMaterials was used for the hardness measurement. Nano-indentation of the material bulk was done prior to the analysis of sub-surface to understand local variations related to multi-phase brass composition. As can be seen in Fig. 3, the hardness distribution was different for the used materials. Alloy CuZn21Si3P contains

Table 1 Chemical composition of the used materials (wt. %)

Alloy	EN code	Type	Cu	Zn	Pb	Sn	Fe	Al	Si	As
CuZn38As	CW511L	α	Rest	37.1	0.12	0.02	0.07	0.02	0.02	0.06
CuZn21Si3P	CW724R	α - κ'	Rest	20.9	0.02	0.03	0.08	0.07	3.2	0.02

Fig. 1 **a** EBSD image showing phase distribution and crystal orientation for CuZn21Si3P. **b** EBSD image showing phase distribution and crystal orientation for CuZn38As. **c** XRD pattern for CuZn21Si3



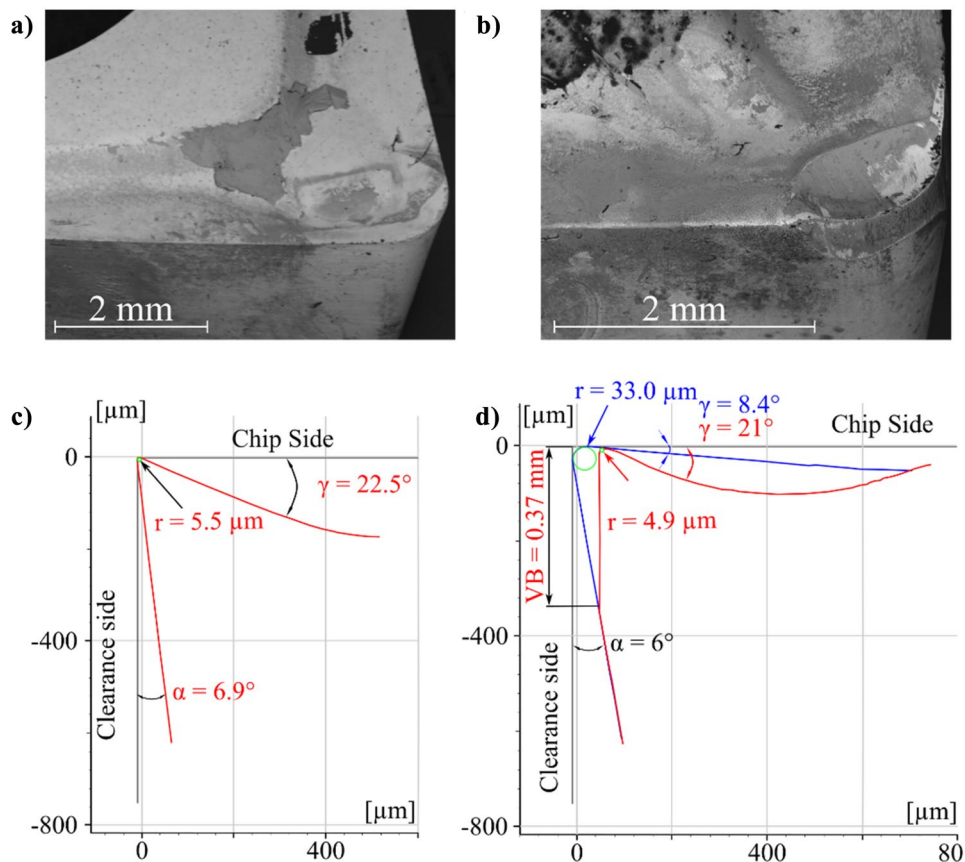
two different phases and shows a wider, non-symmetric hardness distribution as compared to alloy CuZn38As that only contains one phase. The mean hardness value for CuZn21Si3P was 2.6 GPa, and for CuZn38As 1.5 GPa.

To characterize the sub-surface deformation using nano-indentation, 15 indentations were made in depth below the surface, all spaced 15 μm apart. Five indentations were

performed for each depth level, spaced 50 μm apart. Thus, a matrix of 5 by 15 indentations was done for each sample as seen in Fig. 4.

For visualization of the deformation zone, further ion beam polishing of the samples followed by Ion Channeling Contrast Imaging (ICCI) [28] was performed in a FEI Nova 600 Focused Ion Beam/Scanning Electron Microscope (FIB/

Fig. 2 SEM image of the unworn (a) and worn (b) tools together with the cutting edge profile of the unworn (c) and worn (d) tool. For the worn tool, the blue line represents the original edge line profile, and the red line shows the actual worn edge profile



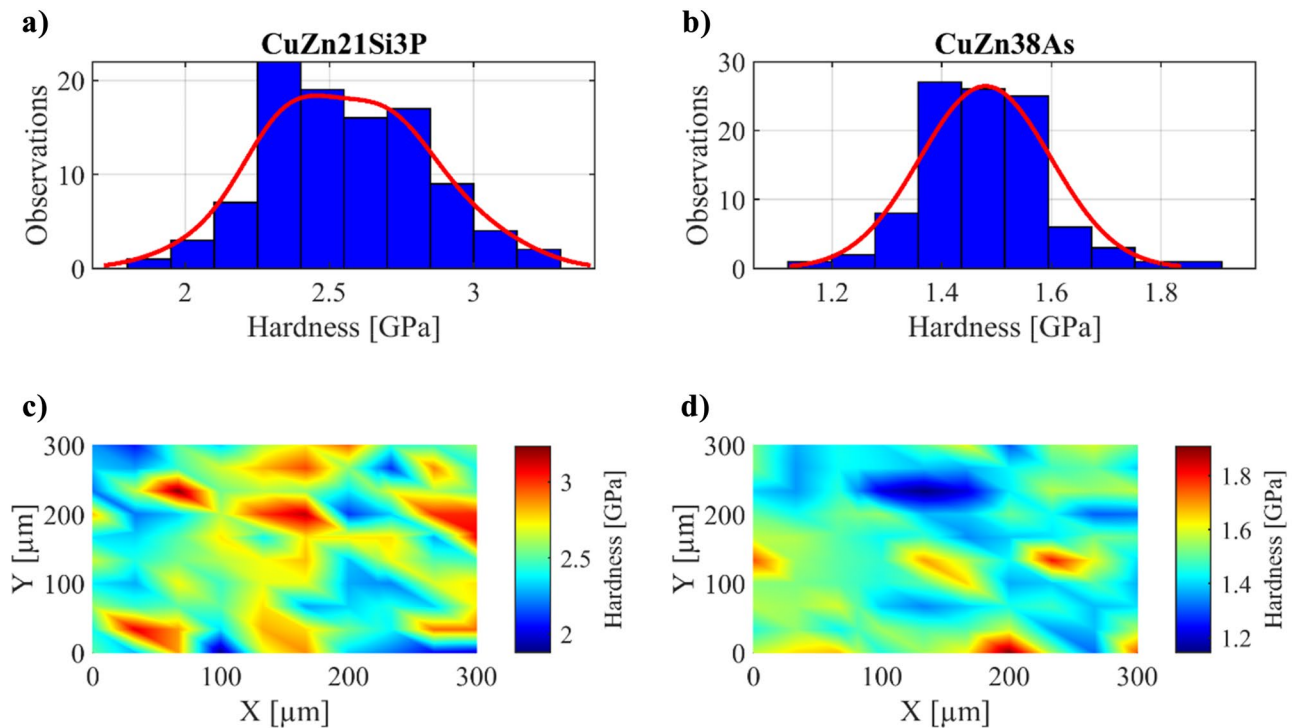
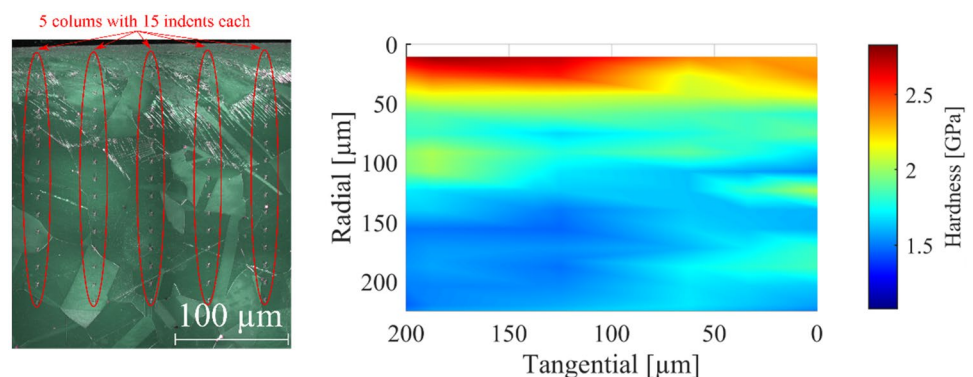


Fig. 3 Hardness distribution in the bulk of the materials (a) and (b) measured in a 10×10 matrix with 30- μm spacing between indents and color-maps showing the hardness distribution in the samples (c) and (d). Note the difference in hardness scale

SEM). ICCI is an imaging technique that provides excellent grain contrast in brass. A JEOL 6490LV SEM with an EBSD detector by Oxford Instrument NordlysMax3 was further used to quantify the microstructure variation in the superficial layer. To evaluate the susceptibility to SCC, accelerated corrosion testing in accordance with SIS 117102 [29] was performed. This test method was chosen because it was developed to evaluate the effect of processing-induced internal stresses in materials without the influence of externally applied stress. For brass and other copper alloys, the susceptibility to SCC is commonly evaluated in accordance with standard ISO 6957 [30], in which an external applied stress is used. That standard is thus not suitable for evaluation of the impact of machining-induced surface integrity

only. Before exposure, test specimens were degreased in acetone and pickled in 5 vol. % sulfuric acid solution. After pickling specimens were rinsed in water and dried in forced hot air convection. The test solution was prepared by adding concentrated ammonia to deionized water. Copper sulphate was dissolved in the ammonia solution followed by dilution with deionized water to final test volume to the concentration 1 mol NH_4OH and 0.05 mol CuSO_4 per liter of test solution. At the start of exposure, test specimens were totally immersed in the test solution at room temperature. The different samples were exposed in separate excicators. Test specimens were taken out from the test solutions for inspection after 30 min to enable evaluation of crack initiation.

Fig. 4 Example of hardness measurement imprints captured using a light optical microscopy in polarized light and mapping of measured hardness for a sample machined using a worn insert at $f=0.4$ mm/rev in alloy CuZn38As



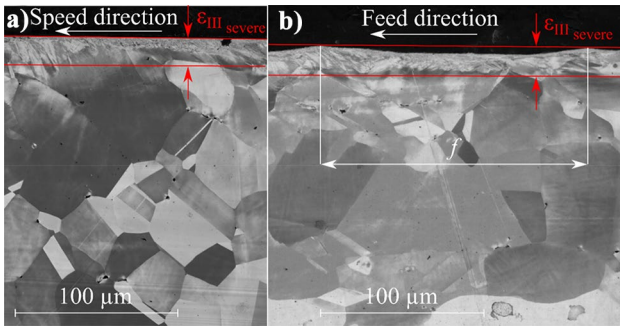


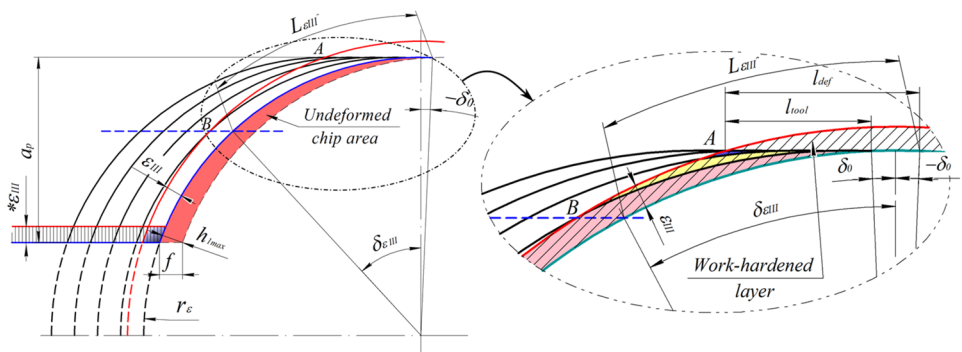
Fig. 5 Ion Channeling Contrast Images (ICCI) after FIB polishing of the deformation zone with the severely deformed part marked by red arrows, for a sample cut in the tangential direction, (a), and a sample cut in the axial direction, (b). The samples of CuZn38As alloy were machined using a sharp insert with $f=0.15$ mm/rev

3 Results and discussion

Longitudinal turning is an anisotropic process where observed characteristics such as topography and sub-surface deformation strongly depend on the viewing direction. When inspecting a cross section of the workpiece seen along the axial direction, the surface is curved according to the workpiece diameter, but no ridges are seen, as in Fig. 5a. When inspecting a cross section of a machined workpiece along the tangential direction, the ridges and valleys created by the tool’s nose radius are visible. The spacing between the ridges is approximately equal to the feed rate, Fig. 5b. Although the surface topography appears different depending on viewing direction, the depth of the severely deformed material ($\epsilon_{III,severe}$ closest to the machined surface) is independent from viewing direction.

Formation of sub-surface deformation—i.e. its depth and degree of work-hardening—is dependent on the thermo-mechanical state of the generated surface. For a given material, it is controlled by cutting conditions, tool geometry and tool wear. It is known that the higher mechanical load caused by a higher feed produces a deeper and more work-hardened layer [31]. Thermal softening under high cutting speeds can facilitate localization of deformation to near-surface layer.

Fig. 6 Schematic of the interaction between sub-surface deformation from single and sequential cuts in longitudinal turning with tools having a nose radius. Adopted from Bushlya et al. [33]



Still, tool wear is among the most defining factors influencing sub-surface deformation and sub-surface damage [32]. This rather predicable and linear behavior becomes much more complicated when machining with cutting tools having a nose radius, $r_ε$ [33]. Sub-surface deformation that is generated during the current cut affects not only machined surface but also the temporary surface, Fig. 6. During the sequential cut, when the tool has moved one feed forward and the workpiece makes one revolution, the cutting tool might cut through already work-hardened layer; thus, multiple deformation might take place. The magnitude of such multiple deformations is controlled by three parameters: tool nose radius— $r_ε$, feed— f and depth of sub-surface deformation from a single cut— ϵ_{III} .

3.1 Quantification of machining induced sub-surface deformation

Involvement of so many parameters makes the surface integrity response to the machining operation rather difficult to predict analytically. While it is expected that machining with low feed should generate lower plastic deformation, in the case of a worn tool a rather comparable sub-surface deformation ϵ_{III} is found for $f=0.05$ mm/rev and $f=0.15$ mm/rev, see Fig. 7. For both machining conditions, the depth of work-hardening is approximately 220 μ m. Still, for low feed of $f=0.05$ mm/rev the surface hardness is higher because the cutting tool passed over the surface several times. When the feed is very large and is bigger than the original ϵ_{III} , the tool will not re-engage with previously deformed layer and will generate lesser overall deformation, as seen in Fig. 8 for $f=0.4$ mm/rev.

The influence of feed rate was not significant in this study; however, the wear condition of the tools was important. An increase of both depth of ϵ_{III} and the severity of work-hardening were seen for the worn tool. The two alloys showed different response to the tool conditions. In Fig. 8, a quotient between the local sub-surface hardness, H , to the unaffected bulk hardness, H_{bulk} , is presented for all cases. For unworn tools, machining of alloy CuZn38As generated

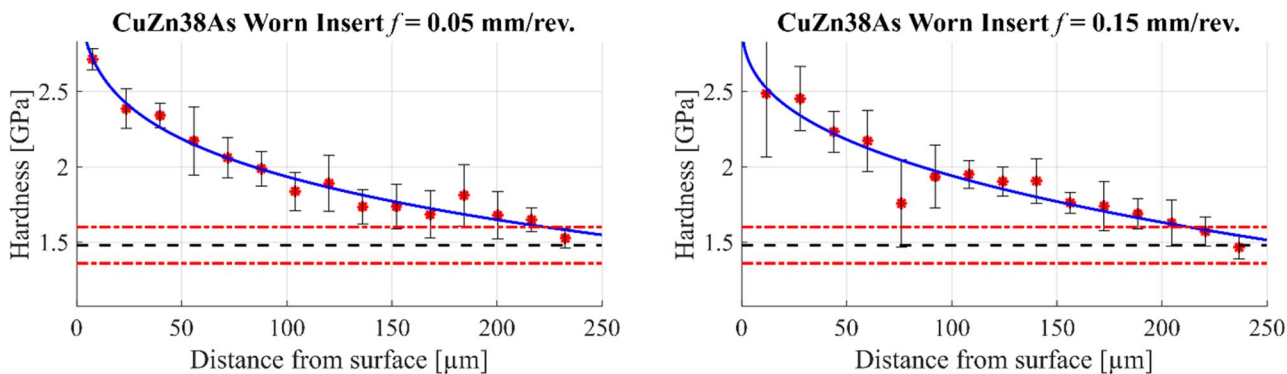


Fig. 7 Hardness distribution for two samples machined with a worn insert and different feed. The red lines show max and min hardness, and the black line shows the average hardness for the unaffected bulk material

nearly twice as deep plastic deformation zone and approx. 20% higher degree of work-hardening compared to the silicon brass CuZn21Si3P. It is worth noting that the depth of work-hardened layer is, as expected, small for low feed condition ($f=0.05$ mm/rev), yet the degree of work-hardening (H/H_{bulk}) is nearly equivalent to the high feed ($f=0.4$ mm/rev) case. As demonstrated in Fig. 6, the case of low feed is accompanied by multiple consecutive cuts over the same sub-surface region, and such multiple deformation then results in a severely deformed but shallow ϵ_{III} layer. Machining with a worn tool gave larger differences between the two alloys. The depth was somewhat comparable for the alloys, yet the work-hardening for CuZn38As was more than 40% higher. The severity of deformation, H/H_{bulk} , for CuZn38As was close to 2, as compared to CuZn21Si3P, where H/H_{bulk} was well below 1.5. In this case, the worn tools induce comparable depth of ϵ_{III} irrespective of feed, since deformation caused by tool geometry dominates over the deformation

caused by feed. However, due to multiple deformations in the cases of low feed a slightly more severe work-hardened layer for $f=0.05$ mm/rev and $f=0.15$ mm/rev is seen in Fig. 8d.

Good correlation was seen between the measured microhardness profiles and the crystallographic misorientation, measured using EBSD, see Fig. 9. Kernel average misorientation analysis was used to evaluate the deformation depth with a step size of $0.5 \mu\text{m}$. The analysis of deformation zone in alloy CuZn21Si3P was less clear, which may be related to the dual phases and the relatively unknown crystallographic arrangement of the κ' phase. It was difficult to obtain Kikuchi diffraction patterns in the severely deformed layer closest to the machined surface, due to excessive deformation which resulted in unresolved black areas. Further investigation of $\epsilon_{III\text{severe}}$ with higher magnification and a step size of $0.05 \mu\text{m}$ revealed that the black area closest to the machined surface had a high fraction of

Fig. 8 The quotient between measured sub-surface hardness and the average hardness of unaffected bulk material for all used machining conditions

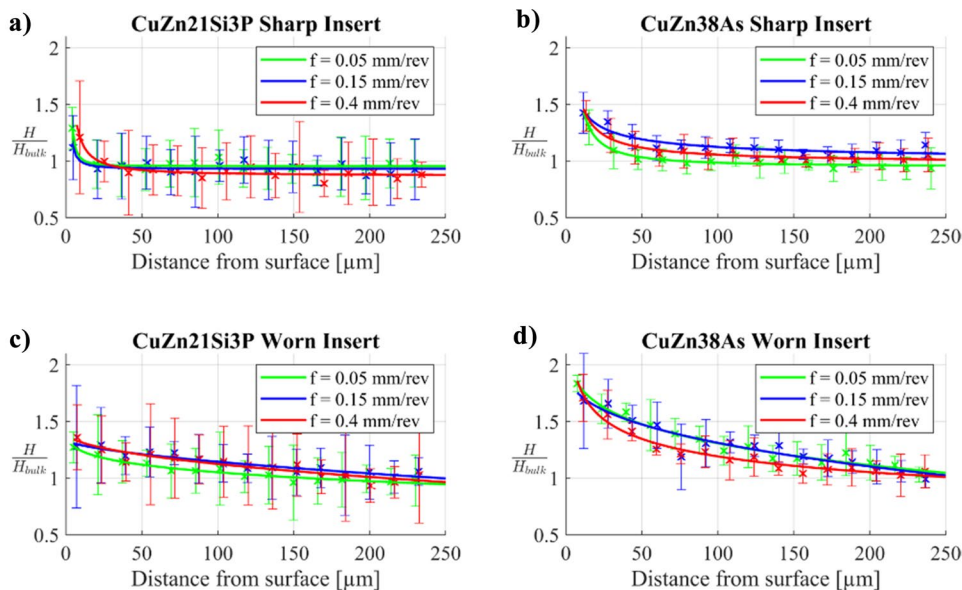
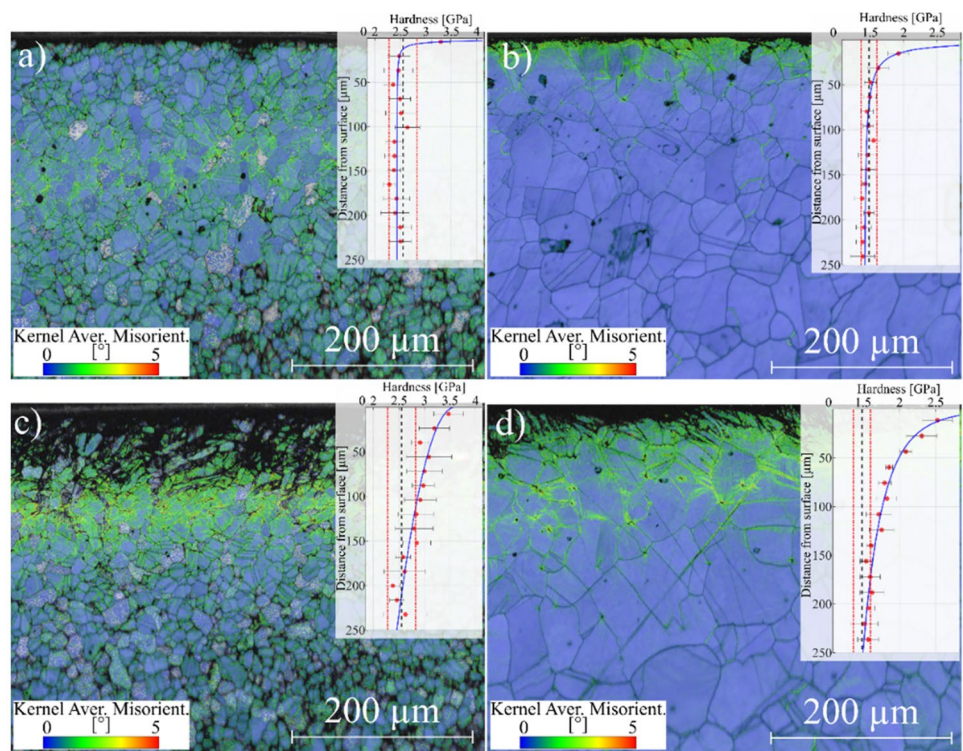


Fig. 9 Kernel average disorientation measured using EBSD overlaid with the hardness profile for the sample, measured with micro indentation. **a** CuZn21Si3P machined with a sharp insert and $f=0.05$ mm/rev, **b** CuZn38As machined with a sharp insert and $f=0.05$ mm/rev, **c** CuZn21Si3P machined with a worn insert and $f=0.4$ mm/rev, **d** CuZn38As machined with a worn insert and $f=0.4$ mm/rev



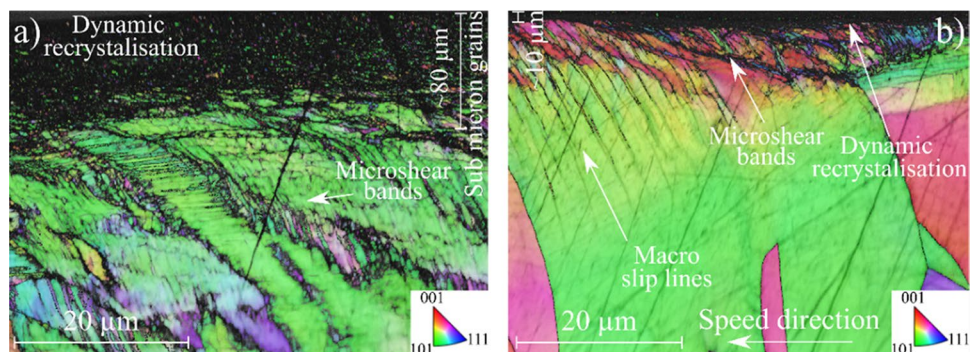
submicron and nano-sized grains, Fig. 10. Formation of such microstructural features in the near-surface region is typically attributed to either severe plastic deformation (SPD) under conditions of high strain and low homologous temperature, T_{hom} , or dynamic recrystallization (DRX) under high strain and high homologous temperature. Dynamic recrystallization typically requires $T/T_{hom} \geq 0.5$ [34], which for brass alloys is equivalent to $T \geq 320$ °C. The temperature when machining these two brass alloys was measured with Infra Red thermal imaging in orthogonal turning following the methodology described elsewhere [35]. Figure 11 shows that the cutting tool temperature is slightly higher than this threshold for sharp tools, and likely even higher for worn tools. Therefore, the submicron grains are likely the result of DRX, while presence of microshear bands is the result of SPD [34], which is related to a gradient temperature reduction deeper into the sub-surface layer, Fig. 10. These

microstructural features and transformations are representative of the so-called white layer which is well studied for machining Ni-alloys and Ti-alloys [18].

3.2 Corrosion

Figure 12 shows optical images of test specimens after corrosion experiments. Compared to the as-machined samples both brass alloys had a more dull appearance after testing. Spots and areas with darker coloration were visible. This appearance was expected since the exposure time was relatively short compared to the maximum exposure time, 48 h, referred to in guidelines to standard SIS 117102 [29]. For alloy CuZn21Si3P, a fraction of the surface had the appearance of corroded striations perpendicular to the cutting speed direction, see Fig. 12. The fraction of corroded surface was higher for a sample machined with a worn tool. For

Fig. 10 EBSD at higher magnification of the severely deformed layer $\epsilon_{III\text{severe}}$ for CuZn38As machined with **a** worn tool and $f=0.4$ mm/rev and **b** sharp tool and $f=0.05$ mm/rev



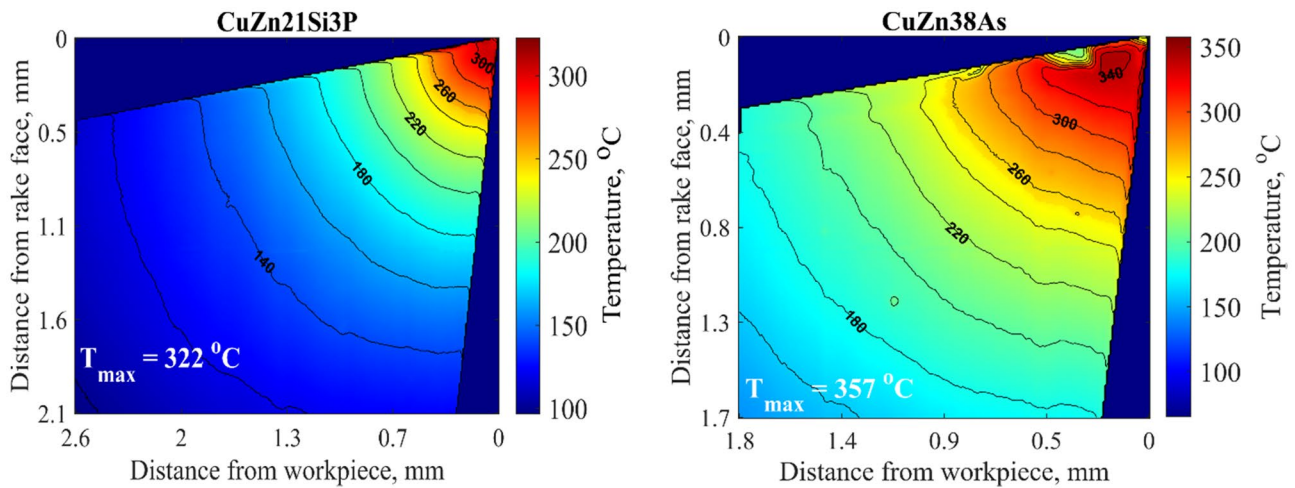
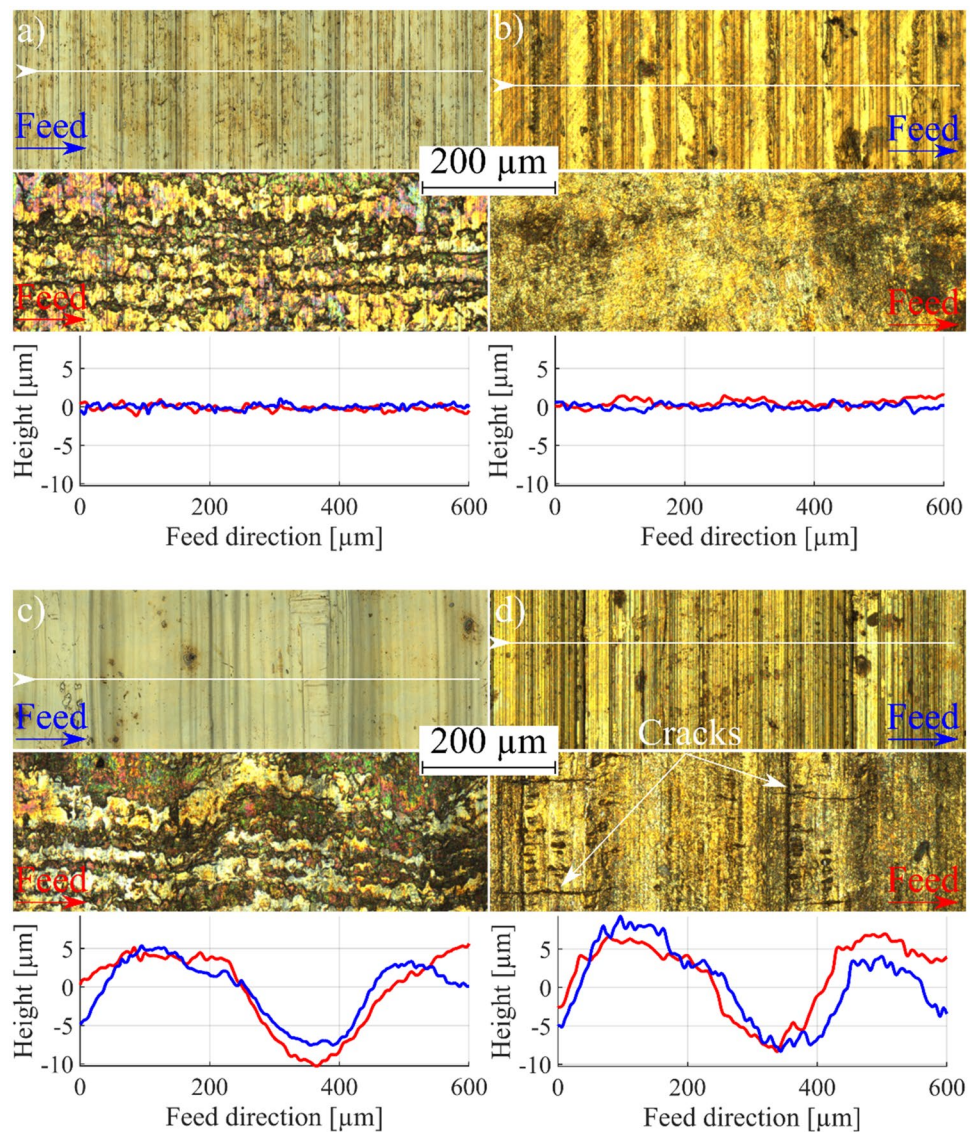


Fig. 11 Tool temperature in orthogonal turning for $f=0.2\text{ mm/rev}$, $a_p=2\text{ mm}$ and $v_c=200\text{ m/min}$. Note the difference in scale between the images

Fig. 12 Optical images of test specimens before (blue) and after 30-min exposure (red) with respective surface profile, measured as indicated by the white arrow. **a** CuZn21Si3P machined with a sharp insert and $f=0.05\text{ mm/rev}$, **b** CuZn38As machined with a sharp insert and $f=0.05\text{ mm/rev}$, **c** CuZn21Si3P machined with a worn insert and $f=0.4\text{ mm/rev}$, **d** CuZn38As machined with a worn insert and $f=0.4\text{ mm/rev}$



alloy CuZn38As, the corrosion striations were not observed, and the surface was affected uniformly. However, the cracks propagating from the surface into the bulk material were present on the CuZn38As sample machined with a worn insert, and also in this case the cracks propagate perpendicularly to the cutting speed direction. The cracks were spaced rather uniformly, approximately 30–50 μm apart, see Fig. 12. The difference in cracking behavior of the alloys cannot be attributed to a difference in the surface topography. Surface roughness before and after exposure was comparable for equivalent feeds and tool wear conditions, as shown by the surface profiles extracted from 3D images in Fig. 12.

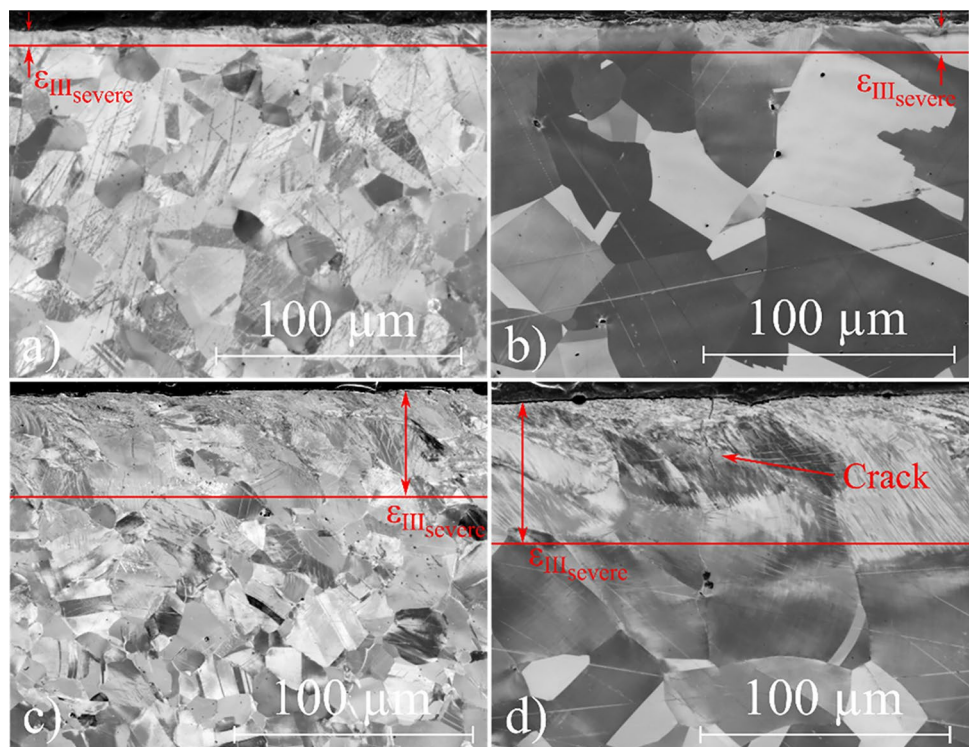
Cross-sectioning of the corroded samples was performed in the cutting speed direction, which was followed by mechanical grinding, polishing and ion beam polishing. ICCI was used to analyze the effect of sub-surface deformation on the stress cracking corrosion, because EBSD was not able to resolve the severely deformed near-surface region (see Fig. 10) where crack initiation and propagation are expected. Despite the very different degree of work-hardening (see Fig. 8) for CuZn21Si3P samples machined with a sharp and worn tools, neither of the samples had cracks, see Fig. 13. The cross section of corroded CuZn38As machined with a sharp tool revealed plastic deformation identical to as-machined samples, but without distinct localized corrosion defects and cracks. On the contrary, CuZn38As sample machined with a worn tool had a series of cracks perpendicular to the surface. Figure 14 shows a detailed view of a crack, which was approximately

45 μm long. The crack originated on the surface and propagated until it met the grain boundary where it was deflected.

The observed behavior of the two brass alloys can be attributed to several different factors. Higher zinc content in alloys is known to increase the susceptibility to SCC [16]. CuZn21Si3P contains 21 wt.% Zn, while the Zn content in CuZn38As is 37 wt. %. Thus, the lower zinc content in CuZn21Si3P is a possible factor behind the absence of cracking in these samples. Still, it is likely that more prolonged exposure of silicon brass will cause cracking. As seen from nano-indentation (Fig. 8), the degree of work-hardening for this alloy was lower compared to CuZn38As; thus, more favorable stress state can be expected. At the same time, silicon brass has nearly 3 times lower thermal conductivity [8], and therefore higher tensile residual stresses are expected [31]. Hence, complementing the surface integrity analysis with analysis of residual stresses should be able to further clarify the observed difference in the accelerated corrosion test.

In this study one sample of each machining condition was exposed to the SIS117102 corrosion test, which makes it difficult to draw definitive and wide-reaching conclusions on the materials resistance to SCC. Additionally, experimenting with machined CuZn21Si3P in prolonged corrosion test could have enabled identification of the defects that initiate stress corrosion cracks. However, our investigation clearly shows that the sub-surface deformation is both deeper and more severe for CuZn38As, compared to CuZn21Si3P, under identical machining conditions. It is also shown that cracks

Fig. 13 **a** CuZn21Si3P machined with a sharp insert and $f=0.05$ mm/rev, **b** CuZn38As machined with a sharp insert and $f=0.05$ mm/rev, **c** CuZn21Si3P machined with a worn insert and $f=0.05$ mm/rev, **d** CuZn38As machined with a worn insert and $f=0.05$ mm/rev showing a crack from the corrosion test



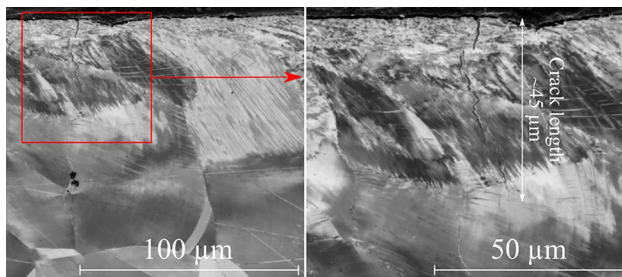


Fig. 14 Detailed view of the crack formation in CuZn38As with a high degree of deformation after machining. The crack is approximately 45 μm deep, and several similar cracks were found in the sample

were only identifiable in CuZn38As machined with a worn insert and $f=0.4$ mm/rev, i.e. the case with the most severe sub-surface deformation. It should be noted that the testing environment according to SIS117102 is dissimilar to real working conditions in order to speed up the reactions. A more accurate impact of surface deformation and residual stresses on SCC is best achieved by extended field exposures. Although very time consuming, such life-time testing can be achieved by comparing test components manufactured with sharp and worn tools installed in active water handling systems.

4 Conclusions

Surface integrity and sub-surface deformation have a significant impact on component performance during the use phase of its life cycle. This paper investigates the sub-surface deformation generated when machining two lead-free brass alloys at three levels of feed rate and under two cutting tool conditions, including a sharp unworn tool and a tool with substantial flank wear.

Analysis of sub-surface deformation revealed only a minor effect of different feed rates but a large influence of the degree of tool wear and cutting edge geometry. Under identical machining conditions, the degree of work-hardening in the CuZn38As alloy was far more severe compared to the CuZn21Si3P alloy but the deformation depth was similar for both alloys. For an unworn tool, the difference in the depth of sub-surface deformation between the alloys was approx. 20%, while for the worn tool the work-hardening variation was as high as 40%.

Stress corrosion cracking of both lead-free brass alloys was assessed by accelerated testing performed according to SIS 117102 standard, in the corrosive environment with 1 mol NH_4OH and 0.05 mol CuSO_4 per liter concentration. After corrosion testing, cracks were found in the most severely deformed sample of CuZn38As machined with a

worn insert and $f=0.4$ mm/rev. This was the case of the most severe case of sub-surface deformation, thus pointing to a link between sub-surface deformation and SCC and highlighting the need for close process control in manufacturing of components to be used in corrosive environments. Higher corrosion resistance of CuZn21Si3P can also be related to a more favorable alloy composition with lower Zn content and dezincification corrosion resistance.

Acknowledgements A special thanks is sent to Klas Holger Jönsson at the Division of Production and Materials Engineering, Lund University for help with sample preparation and Emily Oana Edström at Seco Tools for help with the EBSD analysis.

Author contribution JJ: conceptualization, validation, investigation, methodology, formal analysis, funding acquisition, writing—original draft. VB: methodology, supervision, validation, writing—original draft. CO: conceptualization, validation, investigation, methodology, resources, writing—original draft. RM: formal analysis, investigation, resources. JH: investigation, resources. FL: formal analysis, investigation, validation, writing—original draft.

Funding Open access funding provided by Lund University. This work was funded by the national strategic innovation program—national action for Metallic Materials, organized by Vinnova and Jernkontoret (Sweden) under the Optibrass project (ID 2019–02933) and the Sustainable Production Initiative (SPI), a collaboration between Lund University and Chalmers Institute of Technology.

Availability of data and material The raw/processed data required to reproduce these findings cannot be shared at this time as the data also forms part of an ongoing study.

Code availability Not applicable.

Declarations

Ethics approval Not applicable.

Consent to participate Written informed consent for publication was obtained from all participants.

Consent for publication Written informed consent for publication was obtained from all participants.

Conflict of interest The authors declare no competing interests.

Open Access This article is licensed under a Creative Commons Attribution 4.0 International License, which permits use, sharing, adaptation, distribution and reproduction in any medium or format, as long as you give appropriate credit to the original author(s) and the source, provide a link to the Creative Commons licence, and indicate if changes were made. The images or other third party material in this article are included in the article's Creative Commons licence, unless indicated otherwise in a credit line to the material. If material is not included in the article's Creative Commons licence and your intended use is not permitted by statutory regulation or exceeds the permitted use, you will need to obtain permission directly from the copyright holder. To view a copy of this licence, visit <http://creativecommons.org/licenses/by/4.0/>.

References

- Vilarinho C, Davim JP, Soares D, Castro F, Barbosa J (2005) Influence of the chemical composition on the machinability of brasses. *J Mater Process Technol* 170(1–2):441–447. <https://doi.org/10.1016/j.jmatprotec.2005.05.035>
- Taha MA, E-Mahallawy NA, Mousa TM, Hamouda RM, Yousef AFAG (2012) Microstructure and castability of lead-free silicon brass alloys. *Materialwiss Werkstofftech* 43(8):699–704. <https://doi.org/10.1002/mawe.201200932>
- Estelle AA (2016) Drinking water lead regulations: impact on the brass value chain. *Mater Sci Technol* 32(17):1763–1770. <https://doi.org/10.1080/02670836.2016.1220906>
- Levin R, Zilli Vieira CL, Rosenbaum MH, Bischoff K, Mordarski DC, Brown MJ (2021) The urban lead (Pb) burden in humans, animals and the natural environment. *Environ Res* 193:110377. <https://doi.org/10.1016/j.envres.2020.110377>
- European Union (2020) DIRECTIVE (EU) 2020/2184 OF THE EUROPEAN PARLIAMENT AND OF THE COUNCIL of 16 December 2020 on the quality of water intended for human consumption. Official Journal of the European Union
- Samandi M, Wise M (1989) Machinability of copper based alloys. *J INCRA Rep*. p. 110
- Bushlya V, Johansson D, Lenrick F, Ståhl J-E, Schultheiss F (2017) Wear mechanisms of uncoated and coated cemented carbide tools in machining lead-free silicon brass. *Wear* 376–377:143–151. <https://doi.org/10.1016/j.wear.2017.01.039>
- Johansson J, Persson H, Ståhl JE, Zhou JM, Bushlya V, Schultheiss F (2019) Machinability evaluation of low-lead brass alloys. *Procedia Manufacturing* 38:1723–1730. <https://doi.org/10.1016/j.promfg.2020.01.102>
- Nobel C, Klocke F, Lung D, Wolf S (2014) Machinability enhancement of lead-free brass alloys. *Procedia CIRP* 14:95–100. <https://doi.org/10.1016/j.procir.2014.03.018>
- Tönshoff HK, Arendt C, Amor RB (2000) Cutting of hardened steel. *CIRP Ann* 49(2):547–566. [https://doi.org/10.1016/s0007-8506\(07\)63455-6](https://doi.org/10.1016/s0007-8506(07)63455-6)
- Field M, Kahles JF (1971) Review of surface integrity of machined components. *Annals of the CIRP* 20(2):153–163
- Field M, Kahles JF, Cammet JT (1972) A review of measuring methods for surface integrity. *Annals of the CIRP* 21:219–238
- Brandl E, Malke R, Beck T, Wanner A, Hack T (2009) Stress corrosion cracking and selective corrosion of copper-zinc alloys for the drinking water installation. *Mater Corros* 60(4):251–258. <https://doi.org/10.1002/maco.200805079>
- Bardal E (2004) Corrosion and protection. Springer-Verlag, London
- Sperry ES (1906) The season-cracking of brass and bronze tubing. *Brass World* 2(2):39–44
- Jones RH (2017) Evaluation of stress-corrosion cracking. In R. H. Jones (Ed.), *Stress-corrosion cracking* (pp. 367–417). ASM International. <https://doi.org/10.31399/asm.tb.sccmpe2.t55090367>
- Trent EM, Wright PK (2000) Metal cutting. Butterworth-Heinemann
- Liao ZR, la Monaca A, Murray J, Speidel A, Ushmaev D, Clare A et al (2021) Surface integrity in metal machining—Part I: Fundamentals of surface characteristics and formation mechanisms. *Int J Mach Tools Manuf* 162:103687. <https://doi.org/10.1016/j.ijmactools.2020.103687>
- la Monaca A, Murray JW, Liao Z, Speidel A, Robles-Linares JA, Axinte DA et al (2021) Surface integrity in metal machining—Part II: Functional performance. *Int J Mach Tools Manuf* 164:103718. <https://doi.org/10.1016/j.ijmactools.2021.103718>
- Zhou N, Pettersson R, Peng RL, Schonning M (2016) Effect of surface grinding on chloride induced SCC of 304L. *Materials Science and Engineering a-Structural Materials Properties Microstructure and Processing* 658:50–59. <https://doi.org/10.1016/j.msea.2016.01.078>
- Zhou N, Pettersson R, Schonning M, Peng RL (2018) Influence of surface grinding on corrosion behavior of ferritic stainless steels in boiling magnesium chloride solution. *Mater Corros* 69(11):1560–1571. <https://doi.org/10.1002/maco.201810206>
- Reddy VV, Tam PL, Krishna AV, Rosén BG (2019) Characterization of subsurface deformation of turned brasses: lead brass (CuZn39Pb3) and lead free brass (CuZn21Si3P). *J Phys: Conf Ser* 1183:012006. <https://doi.org/10.1088/1742-6596/1183/1/012006>
- Zoghipour N, Tascioglu E, Atay G, Kaynak Y (2020) Machining-induced surface integrity of holes drilled in lead-free brass alloy. *Procedia CIRP* 87:148–152. ISSN 2212–8271. <https://doi.org/10.1016/j.procir.2020.02.102>
- Metcalfe RG, Pearce-Boltec N (2018) Stress corrosion cracking of a copper elbow fitting. *Eng Fail Anal* 90:197–201. <https://doi.org/10.1016/j.engfailanal.2018.03.016>
- Du XS, Su YJ, Li JX, Qiao LJ, Chu WY (2012) Inhibitive effects and mechanism of phosphates on the stress corrosion cracking of brass in ammonia solutions. *Corros Sci* 60:69–75. <https://doi.org/10.1016/j.corsci.2012.04.011>
- Du XS, Su YJ, Zhang C, Li JX, Qiao LJ, Chu WY et al (2013) Pre-strain enhances film rupture to promote SCC of brass in Mattsson's solution—a proposal for a film-rupture-induced SCC mechanism. *Corros Sci* 69:302–310. <https://doi.org/10.1016/j.corsci.2012.11.043>
- Oliver WC, Pharr GM (1992) An improved technique for determining hardness and elastic-modulus using load and displacement sensing indentation experiments. *J Mater Res* 7(6):1564–1583. <https://doi.org/10.1557/Jmr.1992.1564>
- Giannuzzi LA, Michael JR (2013) Comparison of channeling contrast between ion and electron images. *Microsc Microanal* 19(2):344–349. <https://doi.org/10.1017/S1431927612014286>
- Metallnormcentralen (1970) SIS 117102:1970. Stress corrosion test for copper alloys using ammoniacal copper sulphate solution
- Metallnormcentralen (1988) SS-ISO 6957:1988. Copper alloys—ammonia test for stress corrosion resistance (ISO 6957:1988)
- Ståhl J-E, SecoTools AB (2012) Metal cutting theories and models. *Div Prod Mater Eng*
- Zhou JM, Bushlya V, Peng RL, Johansson S, Avdovic P, Ståhl JE (2011) Effects of tool wear on subsurface deformation of nickel-based superalloy. 1st Cirp Conference on Surface Integrity (Csi) 19:407–413. <https://doi.org/10.1016/j.proeng.2011.11.133>
- Bushlya V, Zhou JM, Ståhl JE (2014) Modeling and experimentation on multistage work-hardening mechanism in machining with nose-radiused tools and its influence on machined subsurface quality and tool wear. *Int J Adv Manuf Technol* 73(1–4):545–555. <https://doi.org/10.1007/s00170-014-5837-0>
- Sakai T, Belyakov A, Kaibyshev R, Miura H, Jonas JJ (2014) Dynamic and post-dynamic recrystallization under hot, cold and severe plastic deformation conditions. *Prog Mater Sci* 60:130–207. <https://doi.org/10.1016/j.pmatsci.2013.09.002>
- Johansson J, Alm P, M'Saoubi R, Malmberg P, Ståhl J-E, Bushlya V (2022) On the function of lead (Pb) in machining brass alloys. *The International Journal of Advanced Manufacturing Technology*. <https://doi.org/10.1007/s00170-022-09205-0>

Publisher's Note Springer Nature remains neutral with regard to jurisdictional claims in published maps and institutional affiliations.